Thermal effects of fluid flow in the Colorado Plateau and the Grand Canyon

Georg-August-University Göttingen
Faculty of Geosciences and Geography
Department of Structural Geology and Geodynamics

Master's thesis

submitted in Partial Fulfillment
of the Requirements for the Degree of
Master of Science (M.Sc.)
in Geoscience

by

Axel Lüders

born on the 18.07.1990 in Hamburg

9. February 2018

Supervisor: Dr. Elco Luijendijk, Dept. of Structural Geology and Geodynamics, Georg-August-University Göttingen, Göttingen, Germany

Co-supervisor: Dr. Matthew Fox, Dept. of Earth Sciences, University College London, London, England

Declaration

Hiermit versichere ich, dass ich die vorliegende Masterarbeit selbständig und nur mit den angegebenen Hilfsmitteln verfasst habe. Alle Passagen, die ich wörtlich oder sinngemäß aus der Literatur oder aus anderen Quellen wie z.B. Internetseiten übernommen habe, habe ich deutlich als Zitat mit Angabe der Quelle kenntlich gemacht. Darüber hinaus versichere ich, dass die eingereichte Arbeit weder vollständig noch in wesentlichen Teilen Gegenstand eines anderen Prüfungsverfahrens gewesen ist. Eine gegebenenfalls eingereichte digitale Version stimmt mit der schriftlichen Fassung überein.

Datum: ______________________ Unterschrift: ______________________

Acknowledgment

In the first place, i am more than grateful of my two supervisors Dr. Elco Luijendijk and Dr. Matthew Fox for providing me the opportunity to carry out this interesting study of numerical modeling of groundwater and heat flow in the Grand Canyon.
Special thanks to supervisor Dr. Elco Luijendijk for introducing me to the modeling with Sutra. Your patience, positive, humorful and motivating way plus your valueable feedback throughout the entire master thesis time helped me a lot. Also, I can't express how grateful I am that you always have an open door for my concerns.
I would also like to express my gratitude to Pascal and Mogens for their friendship, scientific exchange, correction of my master thesis and their support in all matters. Thanks to my office mate Torben for the nice and amusing time. Another thanks goes to Sarah for the correction of my master thesis and useful improvements on my english writing. Phu deserves a special thanks for checking my LaTeX file and having some awesome meals.
And last but not least, I would like to thank my family for their unconditional support and encouragements in this special time.

Abstract

The timing of the formation of the Grand Canyon is still not fully understood, especially 1) whether the Grand Canyon is most recently carved by the Colorado River at 5-6 Ma ago or 2) the Grand Canyon has been formed 70 - 55 Ma ago. Extensive thermochronological measurements could not provide unambiguous age control. The interpretation of thermochronological data depends on geothermal gradients, which can be influenced by groundwater flow. Therefore, information on groundwater and heat flow could provide important constraints on the thermal history of the Grand Canyon. In this thesis I use 2-D numerical model of groundwater and heat flow to infer past and present-day temperature geothermal gradients of the Grand Canyon. I calibrated the model permeabilities using hydrogeological datasets like groundwater recharge and spring discharge.
The results show varying geothermal gradients in time and space. Present-day conditions demonstrate higher geothermal gradients in the area of the Colorado River ($\sim$ 28°C) whereas the areas at higher altitudes show lower geothermal gradients ($\sim$ 10°C) due to cooling effect of groundwater flow. Due to the upwards flow, the area close to the Colorado River is being heated up by $\sim$ 14°C while the largest part of the model is being cooled down up to 32°C. Moreover, this cooling effect increases with higher groundwater recharge values in the Pleistocene. The results indicate that groundwater flow and heat flow data alter the thermal history of the Grand Canyon and therefore should be included in interpretations of the time of formation that rely on low-temperature thermochronology.

Contents

List of Figures

List of Tables

1 Introduction

What is known about the timing of formation of the Grand Canyon is based on numerous studies which have been vigorously debated over nearly a century (*Karlstrom et al.*, 2014). All these theories (whether the oldest or youngest) rely almost exclusively on thermochronological data. Thermochronology methods like apatite fission-track (AFT) data and (U-Th)/He systems can be used to derive the temperature history of specific rocks. Both methods show overlaps for cooling constraints for ranges of temperature. Literature reveal temperatures for AFT at 60 - 110 °C (*Ketcham et al.*, 2007),while the temperature for (U-Th)/He (AHe) dating is classified between 30 - 90 °C (*Farley*, 2000; *Shuster and Farley*, 2004). These temperatures give evidence for the thermal history of the rock which can be derived by means of exhumation. Moreover, the burial depth can be linked to those temperatures. Nevertheless, there has been some disagreement in thermochronological measurements regarding the time of formation of the Grand Canyon. Previous findings have led to a huge gap in the timescale. Several studies underpin the „old" canyon model, but then again a lot of recent researches suggests the „young" canyon model to be accurate. According to *Wernicke* (2011) the former model state that the most of the Grand Canyon was formed by precursor rivers, beginning the process of incision at 80 - 70 Ma years ago, whereas the second one reflects that the Grand Canyon was carved through integration of paleocanyons prior to 6 - 5 Ma years (*Karlstrom et al.*, 2008). For precise cooling times and the associated incision of the Canyon more impact factors should be established to quantify the correct geothermal gradients. One of those impact factors might be the groundwater and heat flow. It is known that the subsurface temperature can change due groundwater flow (*Irvine et al.*, 2015; *Anderson*, 2005; *Keshari and Koo*, 2007). According to *Hill et al.* (2016) the groundwater flow does affect the interpretations of thermochronology. Therefore, it is necessary to gain better insights by means of thermal effects of groundwater and heat flow to obtain geothermal gradients for the Grand Canyon.

The thermal effect is governed by lots of interactions and strongly underlies the permeability of the lithologies (*Gleeson et al.*, 2011). Permeability is decisive for the quantification of groundwater fluxes but varies by more than 13 orders of magnitude and is difficult to determine (*Gleeson et al.*, 2011). Moreover, the heterogeneity, faults and joints in layers in the Grand Canyon constrain the quantification of the permeability. Consequently, the uncertainty of permeability requires a closer inspection of subsurface temperatures of groundwater to classify thermal effects and the related geothermal gradients.

In this study, I use a two-dimensional groundwater and heat flow model (Sutra, version 3.9) along a determined cross-section (Figure 1.1) in the Grand Canyon to quantify present and past fluid flow and its influence on subsurface temperatures. This model aims to improve the knowledge of thermal effects of groundwater and heat flow in the study area.

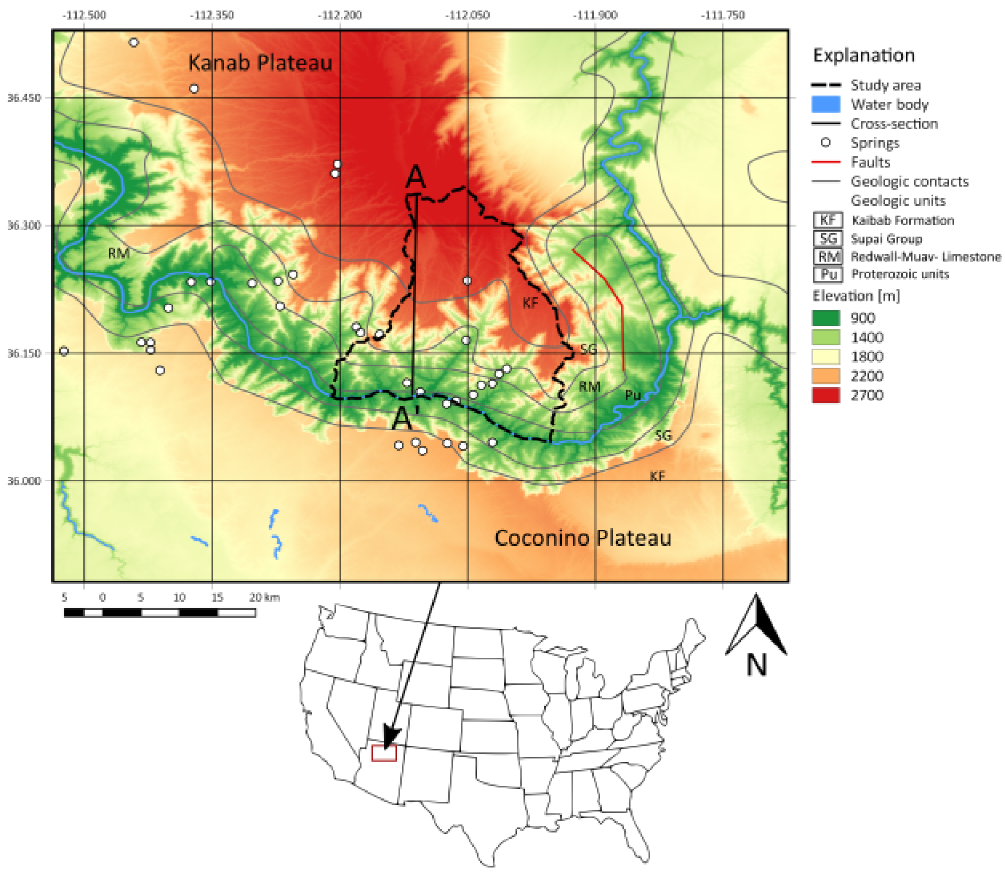

Figure 1.1: Regional geography and topography of the Grand Canyon along the Colorado River as a part of the Colorado Plateau located in the southwestern United States of America. The dotted line demonstrates the restricted area of the study area whereas the line A - A' indicates a cross section. White dots mark the location of springs.

2 Study Area

2.1 Stratigraphy and Lithology

The Grand Canyon is one of the biggest erosional features in the world. It is located in the northwest of Arizona and partly belongs to the Colorado Plateau. The area around the Canyon is subdivided into different parts: The Kanab, Kaibab, Unikaret, Shivwits Plateau in the north and the Hualapei and Coconino part in the south (*Ingraham et al.*, 2001). The study area is located in the Kanab Plateau as shown in Figure 1.1. On average the Grand Canyon is 13 - 16 km wide and more than 1.6 km deep. The steep sided canyon is carved by the Colorado River and exposes stratigraphic sections of Proterozoic and Paleozoic age. However, the geological record from the Ordovician, Silurian, Mesozoic and Cenozoic are missing (*Foos*, 1999). According to *Metzger* (1961), the basement consists of Vishnu Rocks, the oldest rocks in that area, which are intruded by dikes and have been metamorphosed from igneous rocks into gneiss, whereas the overlaying Grand Canyon series consits of deposited sea sediments. The Great Unconformity above the Grand Canyon series separates the Proterozoic from the Paleozoic units. The Paleozoic strata begins from here on and demonstrates a transition from near shore to offshore environments corresponding to transgression which takes place due the global sea-level rise (*Foos*, 1999). The first depositional event includes the units of the Tapeats Sandstone, the Bright Angel Shale and the Muav Limestone that are shown in a Figure 2.1. After periods of lower sea-levels, the marine unit of the Redwall Limestone marks a sea level rise. At the end of the Mississipian age a karst landscape developed. The following unit in the section is the Supai Group which can be dated to the Pennsylvanian and Permian. The sediments are typical for a delta to near shore beach environment. Overlain is the Hermit Formation which shows deposits of a broad coastal plain (*Price*, 1999). Above this layer the Coconino Sandstone with eolian deposits is exposed. The both remaining units, the Toroweap Formation and Kaibab limestone, represent marine units.

Partly exposed in the section of the Grand Canyon are the Triassic sedimentary rock that are subdivided into the Moenkopi formation and the Shinarump formation. For a closer and a more detailed view Figure 2.1 shows the segmentation of layers, the ages and thickness of the respective layers as well as the material compositions.

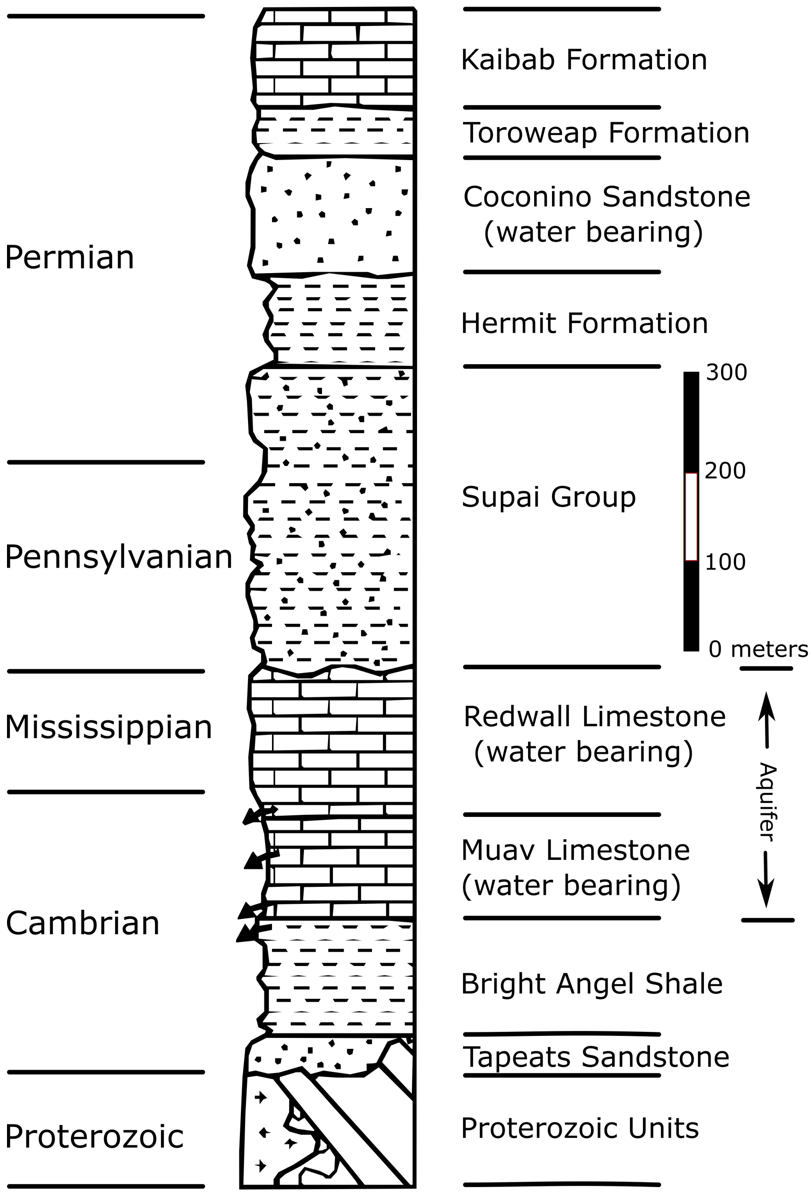

Figure 2.1: Generalized stratigraphic section of the Grand Canyon demonstrating the approximated thickness of the respective layers, water bearing units, the regional Redwall-Muav Aquifer. Modified after *Beus and Morales* (2003).

2.2 Hydrogeology

According to *Hill and Polyak* (2010), the Mississippian Redwall Limestone and the Cambrian Muav Limestone should be highlighted because of their excellent reservoir quality for storing large quantities of water. Both hydro-stratigraphic units can be comprised into one main karstic horizon which is the Redwall-Muav aquifer. Nevertheless, the Coconino limestone can also be seen as a smaller water-bearing unit, which allows the downwards percolation of groundwater (*Metzger*, 1961).
The groundwater flow starts at the surface and descends through fractures and master joints from the uppermost to the units below. The Kaibab Limestone and the Toroweap Formation form sinkholes by dissolution of evaporites. The following underlying Coconino sandstone shows a slightly better hydraulic conductivity in comparison to bordering units, which leads to small quantities of spring discharges through this layer (*Hill and Polyak*, 2010). Beneath the Coconino sandstone the hydraulic conductivity is so low that the groundwater is only able to flow through fractures and faults. Thus, faults and fractures provide pathways for the migrating groundwater down to the Redwall – Muav aquifer. The Bright Angel Fault, is one of those faults that serve as conduit for groundwater discharge, starting at the Coconino Plateau and runing from northeast to southwest and past the North Rim (*Ingraham et al.*, 2001). Several springs can be observed close to the study area, for instance the Roaring Springs in the North Rim (*Huntoon*, 1974). The water-table, which can be observed in the Redwall–Muav aquifer, is featured by a lot of caves which are comprised as unconfined and confined types (*Huntoon*, 2000a,b). The permeable Mississippian paleokarst-breccia horizon extends to the nearly impermeable Bright Angel Shale. This karst system is, compared to the South Rim, extensively developed at the North Rim (*Huntoon*, 2000a). The most part of groundwater recharge that reaches the Redwall-Muav aquifer converge into flows that discharge as springs above the percolation barrier. These include mostly the springs in the study area which are in shown in section 3.1(Figure 3.1).

3 Methods

3.1 Groundwater recharge and spring water budget

The study area is located in the North Rim, a part of the American National Park Grand Canyon in Arizona. The spatial extend of the study area is highlighted by the dark purple and brown colored area in Figure 3.1. The marked area has a surface of 564 km^2. The surface elevation increases from the Colorado River (550 m above sea level) in the south to approximately 2000 m in the north. The study area is separated into two zones, indicated by two different surface types. The purple color marks an area of a flat topography plateau, whereas the brown color marks a landscape with high topographic gradients (Figure 3.1).

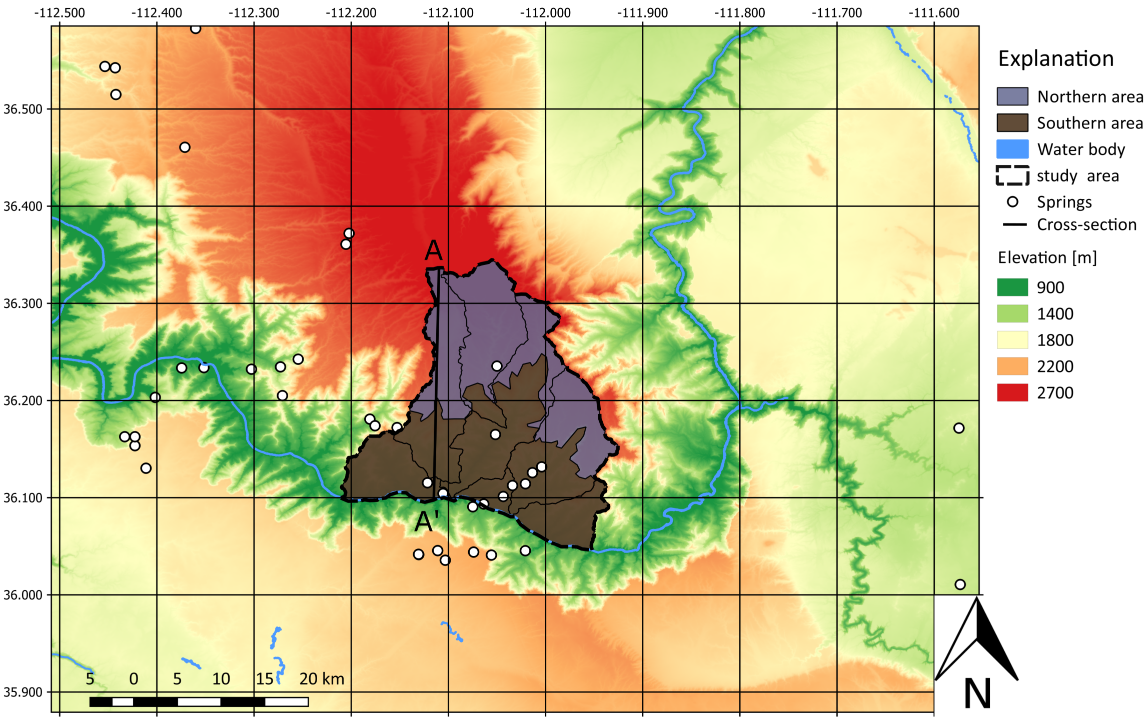

Figure 3.1: Map showing the watersheds of the study area in the Grand Canyon. The area is divided into two parts. The northern area (purple color) represents the higher altitude, whereas the the southern area (brown color) corresponds to the lower altitudes. The National Elevation Dataset(NED) is a raster prodcut assembled by *USGS* (2013). Watershed and high relief data are provided by USGS as well.

For the quantification of the water budget I looked closely at the water system of the whole study area. In general, the sum of inflow minus the sum of outflow correspond to the change in storage. We assume that the water system is in equilibrium and that groundwater inflow is equal to groundwater outflow. Table 3.1 summarizes the groundwater outflow for springs within the study area. Besides measured spring discharges (*ADWR*, 2009) the summed amount is listed. Most of the springs are located close to the Colorado River at lower altitudes (Figure 3.1). Like the surface water, the groundwater flows in a downhill - direction until the water encounters a non-permeable geologic unit and discharges above it. Here, the Bright Angel Shale stands for the Aquiclude. Contributing areas of the springs are mapped for the study area. The drawn lines within the study area correspond to the related watersheds for the springs. Moreover, the discharge of groundwater in this water system is not only restricted to springs, but can also discharge through the Colorado River.

Table 3.1: Discharge measurements for several springs in the study area based on (*ADWR*, 2009).

Springs	Q - Discharge (m^3 yr^{-1})
Angel	1.55 x 10^7
Roaring	3.88 x 10^6
Dragon	1.25 x 10^6
Haunted	8.56 x 10^5
Crystal	4.91 x 10^5
Emmet	4.28 x 10^5
Ribbon	3.66 x 10^5
North Canyon	2.15 x 10^5
Robber′s Roost	1.11 x 10^5
Transcept	1.07 x 10^5
Sum	2.32 x 10^7

3.2 Groundwater and heat flow model

3.2.1 Groundwater and heat flow model equations

In this thesis, I use the two-dimensional numerical model SUTRA (Saturated-Unsaturated Transport)(*Voss and Provost*, 2010) to investigate the groundwater and heatflow in the Grand Canyon and their thermal effects on subsurface temperatures. SUTRA is able to model the fluid flow as well as heat transport in the subsurface.

Numerical procedures are based on finite-elements and the finite-difference method. For the simulation of groundwater and heat flow the model code is built on two fundamental equations: 1) groundwater flow through numerical solution of a fluid-mass-balance equation; and 2) heat transport, which is simulated through numerical solution of an energy-balance equation.

A simplified form for the fluid mass balance can be written as:

$$S_o \frac{\partial h}{\partial t} - \nabla(K \nabla h) = Q^* \qquad \text{eq. 3.1}$$

where $Q^* = (\frac{Q_p}{\rho})$

and S$_o$(x,y)describes the specific storativity [m^{-1}], h(x,y,t) is the hydraulic head as a sum of pressure head and elevation head [m], t is the time [s], K(x,y) is the hydraulic conductivity [m s^{-1}], Q^*(x,y) is the volumetric fluid source[s^{-1}], Q$_\rho$(x,y) is the fluid mass source[kg/(m^3 s)] with a more detailed description of the (mass fluid injected per time/volume aquifer) and ρ is the fluid density [kg/m^3]. The equation is used under the assumption of saturated conditions. Further assumptions are the constant solute concentration and the constant fluid density, and using the definition of hydraulic conductivity, $K \equiv (k\rho g)/\mu$, where g represents the acceleration of gravity. The hydraulic head is defined as $h \equiv h_p$ + ELEVATION, where the pressure head, $h_p \equiv p/(\rho g)$ (*Voss and Provost*, 2010). The energy-balance is expressed as:

$$\begin{aligned} \frac{\partial[\rho e_w + (1-\epsilon)\rho_s e_s]}{\partial t} &= -\nabla(\rho e_w v) + \nabla \cdot [\mu I \cdot \nabla T] + \nabla \cdot [\rho c_w D \cdot \nabla T] \\ &+ Q_p c_w T^* + \rho \gamma_o^w + (1-\epsilon)\rho_s \gamma_o^s \end{aligned} \qquad \text{eq. 3.2}$$

where the first expression on left side of the equal-sign stands for the change of energy in the solid matrix and the fluid over a period of time. The stored energy for a particular volume are expressed by variables of e_W is the energy per unit mass water [kg m^2 s^{-2}/kg], e_s is the energy per unit mass solid matrix [kg m^2 s^{-2}/kg] and ρe_s is the density of solid grain in solid matrix [kg/m^3].
Following terms can influence the stored energy with time: $\lambda(x, y[, z], t)$ is the bulk thermal conductivity of solid matrix plus fluid [kg m^2 s^{-2}/(s·m·°C)], I is the dimensionless identy tensor, c_w is the specific heat of water [kg m^2 s^{-2}/kg·°C], D is the dispersions tensor [m^2/s], T^*(x,y[,z],t) is the temperature of the source fluid [°C],Y_w 0(x,y[,z],t) is the energy source in the fluid [kg m^2 s^{-2}/(kg $\cdot s$)], Y_s 0(x,y[,z],t) is the energy source in the solid grains [kg m^2 s^{-2}/(kg· s)]. The term of Q_p expresses the energy production which are added due to the fluid source with temperature Q^*.
Figure 3.2 shows a simplified geometry of the model that is based on the defined cross-section. The required boundary conditions include that the cross-section is being perpendicular to the axis of the geologic units as well as the spatial proximity of springs. The profile has a length of 23700 m from south to north while the maximum height in the northern part of the cross-section is nearly 2800 m. As shown in Figure 2.1, the model domain is determined by different lithologic units and boundary conditions (see section 2.1). Figure

3.1 show several arrows which indicate the intended flow direction. To quantify this flow behaviour I focus in particular on influecing factors of the permeability and the groundwater recharge. The latter approach is favoured by the fact that the permeability represents a part of hydraulic conductivity (*Freeze and Cherry*, 1979) and therefore is linked to heterogeneity of the porous material (*Durner*, 1994). The groundwater recharge, in turn, shows a large reliance on the climatological conditions over the related period of time. Furthermore, the topography effect of the study area is also relevant to the groundwater recharge, as groundwater can trickle away into the ground or a surface runoff takes place (see section 3.1 for further explanations). Likewise, the permeability of each lithological unit is also debated in section 3.2.2.

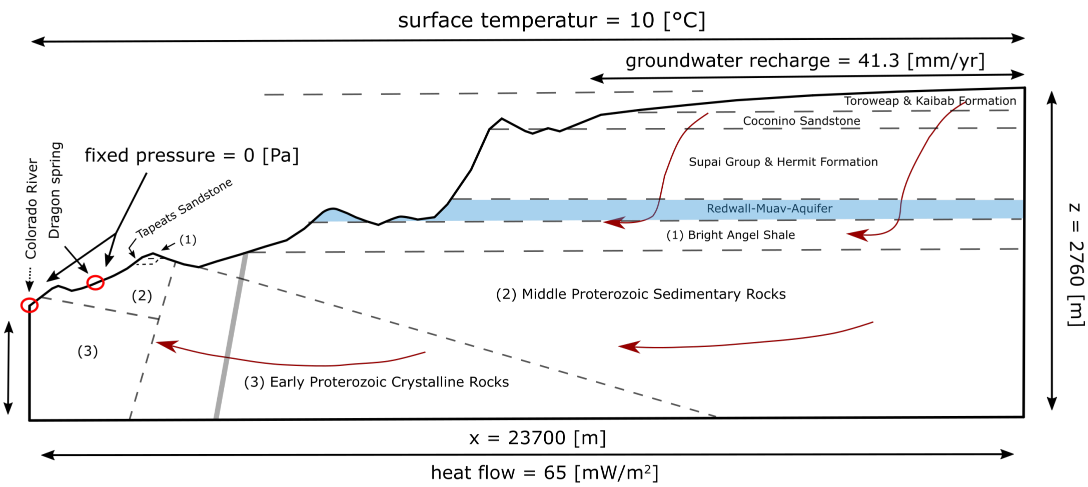

Figure 3.2: Sketch showing the model setup and the adjacent boundary conditions that are present along the identified cross-section.

3.2.2 Permeabilites of lithologic units

Considering the hydraulic characteristics of the lithostratigraphical units, the permeability of porous media is relevant to quantify the groundwater flow. *Kozeny* (1927) and *Carman* (1937) show that the expression of permeability is related to the porosity and the pore size. By setting the porosity to a fixed value of 10% for each cell simplifies the simulation and calibration of the permeability. Nevertheless, permeability is difficult to quantify, especially if one considers that the orders of magnitude ranges over more than 13 and that flow direction depends on the heterogeneity (*Gleeson et al.*, 2011; *Freeze and Cherry*, 1979). In this study, the permeabilities at regional scales are quantified by the numerical model. *Gleeson et al.* (2011) provide geometric mean of permeability values for hydrolithologies and combined hydrolithologies in regional-scale. Based on their dataset, I was able to adjust the permeability for the lithologies in the numerical model. The datasets serve as initial values for the permeabilities of our layers. With exception of the shale component the second column of Table 3.2 summarizes the geometric mean logarithmic permeability by *Gleeson et al.* (2011). The permeability value for the shale in this column is provided by *Neuzil* (1994). The third column lists the standard deviations, which are related to values of Column 1. Additionally, the fault zone (see Figure 3.2 and 3.3) have to be considered. According to *Bense et al.* (2013), the permeability of a fault adjacent to their rock can decrease by 2-3 orders of magnitude. This can lead to strong hydrogeological heterogeneities. The final adjustments of my best model fit are conducted by means of numerical modelling in Sutra and are shown in Table 4.2.

Table 3.2: Geometric mean logarithmic permeabilities for model adjustments and standard deviations based on references of 1 = (*Gleeson et al.*, 2011), 2 = (*Neuzil*, 1994).

Lithology	**logk (m^2)**	σ	**References**
Toroweap & Kaibab Formation	-15.2	2.5	1
Coconino & Tapeats Sandstone	-12.9	0.9	1
Supai Group & Hermit Formation	-15.2	2.5	1
Redwall-Muav Aquifer	-11.8	1.5	1
Bright Angle Shale	-19	–	2
Tapeats Sandstone	-12.9	0.9	1
Middle Proterozoic Sedimentary Rocks	-15.2	2.5	1
Early Proterozoic Crystalline Rocks	-14.1	1.5	1

3.2.3 Model boundaries and initial conditions

In the calibrated numerical model the thermal boundary conditions are imposed at (1) the top of the model, temperature (T) = 10°C, which is derived as specified average annual surface temperature for the entire upper model boundary; and (2) at the bottom of the model a constant heat flow of 65 mW s^{-2} is assigned (*Pollack et al.*, 1993). The left and the right model sides do not exhibit boundary conditions. The boundary conditions for the groundwater are applied along the flat plateau area of the model (further explanations are mentioned in the subchapter below). For a better understanding Figure 3.2 demonstrates, among other things, the setup for the boundary conditions.

3.2.3.1 Groundwater recharge

The groundwater recharge is one of those input data that plays a decisive role for the quantification of groundwater and heat flow, but is strongly influenced by the local climate conditions. As reported by *Kumar* (2012), the direct effect of climate change on groundwater depends on changes in volume and the distribution of groundwater recharge. The volume income for groundwater recharge is related to precipitation amounts, intensity rates and timing which indirectly affects the flux in subsurface.

With respect to the boundary condition, the groundwater recharge at the surface is divided into two zones (see Figure 3.1). From x = 9050 m to 23700 m of the model, I have assigned a constant value for groundwater recharge. In contrast, no groundwater recharge is assigned from x = 0 m up to 9050 m, assuming that most of the precipitation in areas with a high topographic gradient is converted to surface runoff.

The literature values from *De Graaf et al.* (2015) represent a steady-state recharge input over the time period of 1957 – 2002. According to this simplified high-resolution global-scale groundwater model the average groundwater recharge for present-day is 5 mm y^{-1}. The extremely low recharge rates are due the arid climate conditions.
For applications in Sutra I used a groundwater recharge of 41.3 mm y^{-1}, which are calculated on the basis of measured spring discharges (also discussed in section 4.1). Additionally, other literature values of groundwater recharge used are shown in Table 4.1.

3.2.4 Model discretization

The model simulation is based on a simplified two-dimensional-geometry. The mentioned equations (3.1) & (3.2) for the groundwater and heat flow are solved along the 2D-model. The model length is set to 23700 m in x-direction, while the height of the model domain reaches 2760 m in $z-$direction. The topography of the cross-section which is described by the upper boundary varies from 750 m on the model's left side up to 2760 m at the model's right side as shown in Figure 3.3. To obtain a good fit for the topography given cross-section of QGIS (Figure 1.1) I use 20 rectangles consisting of grid cells. The 20 rectangles were subdivided in rows and columns. The cell size in width ranges from a minimum of 20 m to a maximum of 42 m per cell (Figure 3.3). The height of each cell varies from 7.5 m up to 27.5 m.

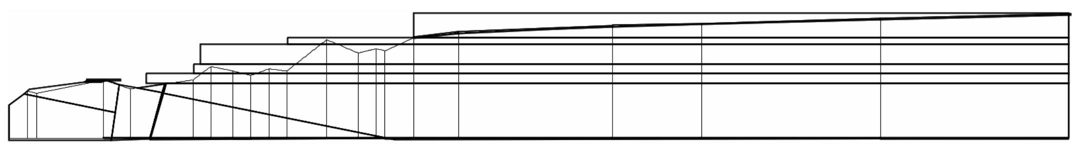

Figure 3.3: Model domain contains stratigraphic units in simplified vertical extent and mentioned horizontal lines which divide the rectangles. Not included are the element outlines.

The lithostratigraphic units in the model are in sequence from bottom to top the Early Proterozoic Sedimentary Rocks, Middle Proterozoic Sedimentary Rocks, the Bright Angle Shale, the Mississipian Redwall Muav, the Supai Group & Hermit Formation, the Coconino sandstone and the Toroweap & Kaibab Formation (see Figure 2.1). In contrast to the younger and horizontal layers, the older proterozoic layers are dipping down at an angle of $\sim 35°$. Besides this layout, the grey marked line in Figure 3.2 represents a fault zone. Regarding the time discretization, the modeled time steps for paleozoic and present-day are set to 1 year to compare simulation results of equal stratigraphic settings under different recharge conditions.

3.2.5 Model calibration

The model calibration serves to optimize the numerical simulation of the thermal effects of the groundwater and heat flow and the possible implications on thermochronological datasets. First model simulations are focused on setting up a scenario which corresponds

to the present-day conditions. To ensure that the enviromental conditions reflect the actual situation, I imported the related discretization of the determined cross-section from the study area into Sutra. Subsequently, I added parameters such as groundwater recharge, heat flow, porosity and thermal conductivty values. For the model calibration, values of groundwater recharge, discharge and permeability are of vital importance. On the basis of measured spring discharge (*ADWR*, 2009) and modeled groundwater recharge values I calibrated the permeability for each lithologic unit.
First attempts are based on the initial permeabilites of lithologic units given by *Gleeson et al.* (2011); *Neuzil* (1994). Given the high uncertainty of permeability, the standard deviations are also taken into account. Moreover, I conducted a parameter study for the permeability to evaluate the impact of varying permeability rates.
Further scenarios deal with the influencing factors such as the porosity and thermal conductivity. For the porosity I simulated scenarios with initial values of 5% and 30%, whereas the thermal conductivity are examined for values of 1.5 and 4. The great range of values should provide a preferably great impact on the thermal effects.

3.2.6 Groundwater flow in the Pleistocene

Initially, the first scenario measurements are related to the present-day values whereas the following scenarios intend to examine prior data with past fluid flows from the Pleistocene. Additionally, the evolution of groundwater and heatflow over a period of time provide useful insights regarding the thermal effects. On the basis of data from *Zhu et al.* (2003) the paleorecharge rates for the Pleistocene were 2 to 3 times higher than nowadays. The studies on early paleorecharges are based on chloride mass balance method and chlorine-36 data and are made for the area of the Yucca Mountain in Nevada. The knowledge of the paleoclimate changes underpin previous assumptions about the groundwater recharge rates (*Zhu et al.*, 1998). Therefore, I set up model scenarios with 2 to 3 times higher recharge values of present-day conditions. Scenarios with 4 to 5 times higher groundwater recharge values provide a further evolution of the thermal effects of groundwater and heat flow and possible implications for the time of formation of the Grand Canyon.

4 Results

4.1 Spring water budget

Calculations of the actual recharge based on the discharge measurements (*ADWR*, 2009) are shown in Table 3.1. Dividing the sum of the spring discharge by the contributing area results in a value of 41.3 mm yr^{-1} as shown in Table 4.1. For a suitable unit, the term is converted into mm yr^{-1}. Models by *De Graaf et al.* (2015) and *Wolock* (2003) show much lower groundwater recharge values and their estimates are based on a simplified global-scale groundwater model with a 1-kilometer resolution raster. The values in Table 4.1 for the processed areas can be better explained. The lower altitudes in the southern part of the study area are mostly dominated by slopes that hinder the percolation of groundwater and results in runoff. Therefore the recharge value for the southern area is lower than the value for the northern area which can be characterized as relatively flat plateau. In addition, the variation between the measured values of recharge 41.3 mm yr^{-1} and the modeled values of recharge 14.3 and 5 mm yr^{-1} makes it clear that global scale models of *De Graaf et al.* (2015) and *Wolock* (2003) does not fit for this model simulations.

Table 4.1: Calculated groundwater recharge values for specific areas of the study area based on references of 1 = (*De Graaf et al.*, 2015), 2 = (*Wolock*, 2003) and 3 = (*ADWR*, 2009). The location of areas A & B can be found in Figure 3.1.

Area	Groundwater recharge (mm yr^{-1})	References
A & B	5	1
A & B	14.3	2
A	15.8	2
B	13.2	2
A & B	41.3 [(2)]	3

[1] 564000 km^2
[2] Sum of Table 3.1 devided by the area(1)

4.2 Simulations for the model calibration

The measured to calibrated spring discharge of the Dragon spring with values of 3.96 x 10^{-5} m^3 s^{-1} to 3.96 x 10^{-5} m^3 s^{-1} agree well with each other. Best estimates of permeabilities for the calibration of discharge are listed in Table 4.2. In addition to the geologic unis, the permeability value of -13.5 for the fault zone is also shown.

Table 4.2: Permeability values for lithologic units for the best model fit. Initial Geometric mean logarithmic permeabilities and initial standard deviations and the Fault Zone based on references of 1 = (*Gleeson et al.*, 2011), 2 = (*Neuzil*, 1994), 3 = (*Bense et al.*, 2013).

Lithology	**logk (m^2)** calibrated	**logk (m^2)** inital	σ inital	**References** for initial k
Toroweap & Kaibab Formation	-15.9	-15.2	2.5	1
Coconino & Tapeats Sandstone	-13.4	-12.9	0.9	1
Supai Group & Hermit Formation	-15.9	-15.2	2.5	1
Redwall-Muav Aquifer	-10.3	-11.8	1.5	1
Bright Angle Shale	-18.6	-19	–	2
Tapeats Sandstone	-13.4	-12.9	0.9	1
Middle Proterozoic Sedimentary Rocks	-15.34	-15.2	2.5	1
Early Proterozoic Crystalline Rocks	-14.3	-14.1	1.5	1
Fault Zone	-13.5	–	–	3

The following results represent a quantification of the best model fit as well as the influence of different parameters for the thermal effects of the entire model system. Figure 4.1 and 4.3 show the output of model temperatures, permeabilities and flow vectors for the calibrated 2D-cross-section model. The temperature field indicates a consistent horizontal temperature gradation for almost the entire model length with exception of the area close to the Colorado River, which describes an upwards trend towards the discharge sources.

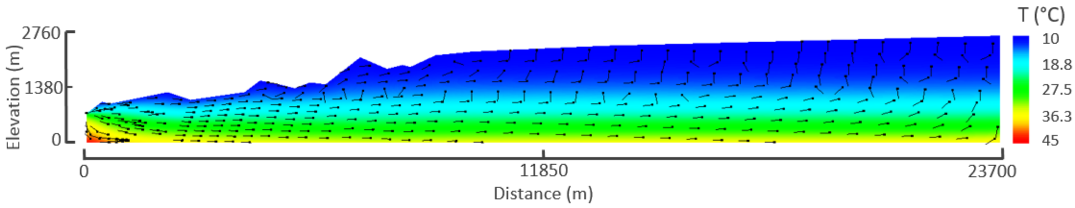

Figure 4.1: Best-calibrated model simulation for the 2D-cross-section from the study area, showing the temperature profile with groundwater recharge conditions at present-day. The flow vectors indicate the groundwater flow directions.

The temperature increase with depth ranges from 10 °C to 36 °C on the right side to ∼ 25 °C to nearly 45 °C on the left side. However, it should be noted that the left side only has an elevation of approximately 800 m, whereas the right side is more than 2700 m high. The observed temperature differences in Figure 4.1 lead to higher geothermal gradients in the discharge area near to the Colorado River compared to the plateau area. Calculated geothermal gradients for locations of x = 0 m and x = 23490 m are ∼ 28 °C/km versus ∼

10 °C/km verify these observations. Figure 4.2 validate the temperature evolution along the model domain. Graphs (a) and (b) show the subsurface temperature - depth relation for the best model fit scenario at positions of x = 0 m and x = 23700 m. Both graphs show lower temperatures at greater depth and increasing temperatures at lower depths. The temperature-depth curve in graph (a) is negative and reaches higher temperature at the surface. In comparison, the curve in graph (b) is positive and reaches slightly lower temperatures at the surface. This difference in fluid temperature over depth is due to the limited groundwater recharge in the plateau area. As shown in Figure 4.1, groundwater recharge and the downwards directed groundwater flow is represented by the flow vectors which are restricted to the uppermost part of the model over the distance of x = 8000 m to 23700 m. In the transition zone visualized by the color change from blue to turquoise the flow vectors change their flow direction towards the discharge area in the left. The reason for this change in orientation of the flow vectors is due the aquiclude (Bright Angel Shale), which is located above the turquoise layer. The lower amount of percolated groundwater through the aquiclude flows in higher permeable units towards the area of the Colorado River. The groundwater flow with an upwards trend in this area is highlighted in a larger scale in Figure 4.3. The observed temperature increase in this area is due to the upwards flow of discharge areas like the Dragon spring (2) and the Colorado River (1) at the left margin.

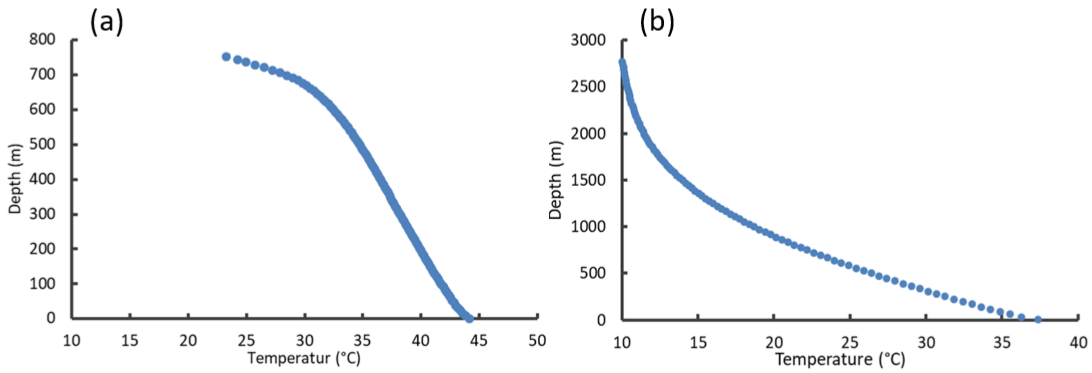

Figure 4.2: Comparison of temperature-depth relations in the model at position (a) x = 0 m and (b) x = 23490 m.

Figure 4.4 illustrates the influence of different permeabilities for four specific geologic units on discharge to the Colorado River and the Dragon spring. Changing the values of permeabilities of the geologic units of Redwall-Muav-Aquifer (a), Bright Angle Shale (b) and the Early Proterozoic Sedimentary Rocks (d) show no influence on the discharge of the Dragon-spring and the Colorado River. The Middle Proterozoic Sedimentary Rocks show an exception with regard to interactions between permeability and discharge. With increasing permeability, logk values under -13.9 lead to a discharge of groundwater into the Colorado River.

Comparing the calibrated best model fit scenario with Figure 4.5 helps to understand the evolution of modeled temperature with and without groundwater recharge. In contrast

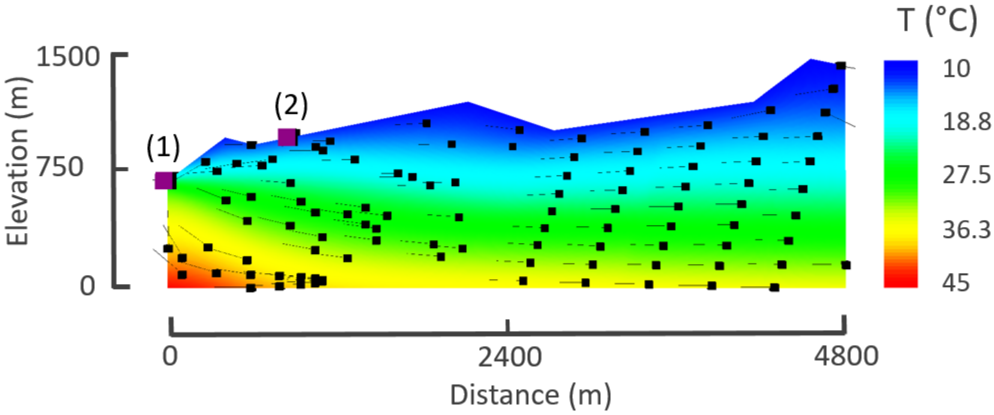

Figure 4.3: Section of the discharge area with locations of the Colorado River (1) and the Dragon spring (2). Best-calibrated model simulation showing the temperature profile with groundwater recharge conditions at present-day and flow vectors for the groundwater flow direction.

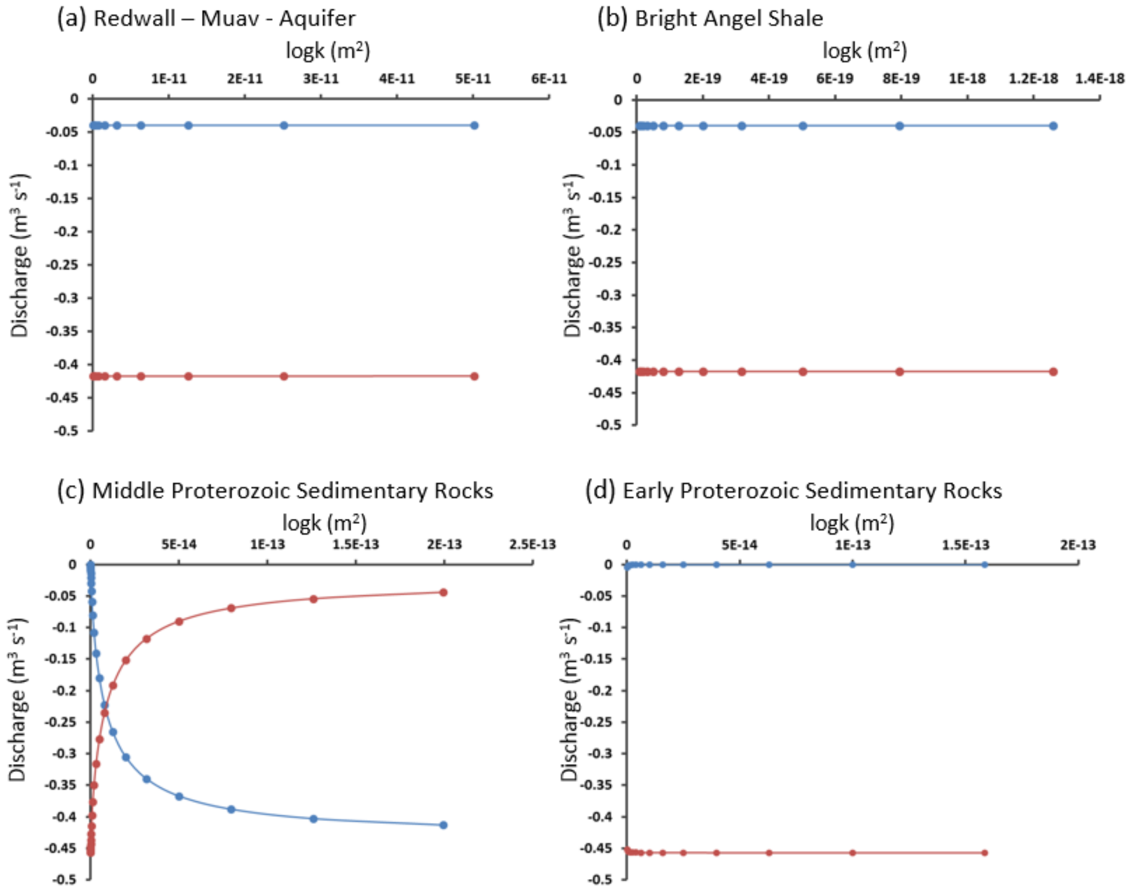

Figure 4.4: The relation between discharge of the Dragon Spring (blue) and the Colorado River (red) to Permeability for specific lithologic units (a) Redwall-Muav-Aquifer, (b) Bright Angle Shale, (c) Early Proterozoic Sedimentary Rocks and (d) Middle Proterozoic Sedimentary Rocks. The Permeability is plotted on the x-axis and the discharge is plotted on the y-axis. The blue dots, which are connected with lines, show calculated discharge values of several permeability settings for the Dragon spring, whereas the red dots represent the Colorado River.

to the first mentioned scenario Figure 4.5, shows a linear temperature field, where the whole system is only controlled by heat conduction. The comparison of both scenarios clearly illustrates cooling effects of groundwater flow on the Colorado Plateau and heating of groundwater near the discharge zones.

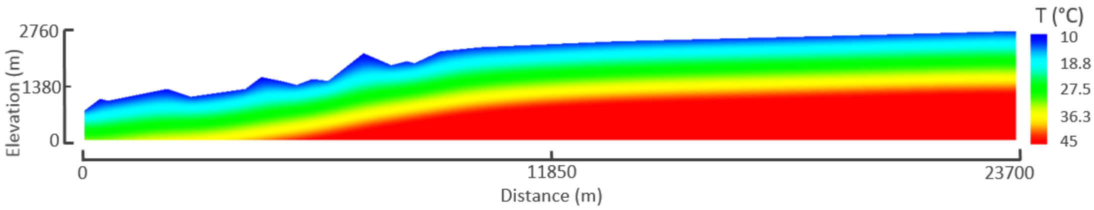

Figure 4.5: Modeled temperature trend for groundwater recharge scenario = 0 mm yr^{-1}.

The comparison of a groundwater recharge and a non-groundwater recharge scenario is shown in temperature difference over depth plots for the left (a) and right side (b) of the model domain(see Figure 4.6). Graph (a) shows that the differences in temperature vary between 10 to 14°C over a depth of 800 m. Graph (b) depicts a difference of temperature values of up to -32°C over a depth of 2800 m. Therefore, the left-hand side of the model is warmer in the groundwater flow scenario, whereas the right-hand side of the model is cooler.

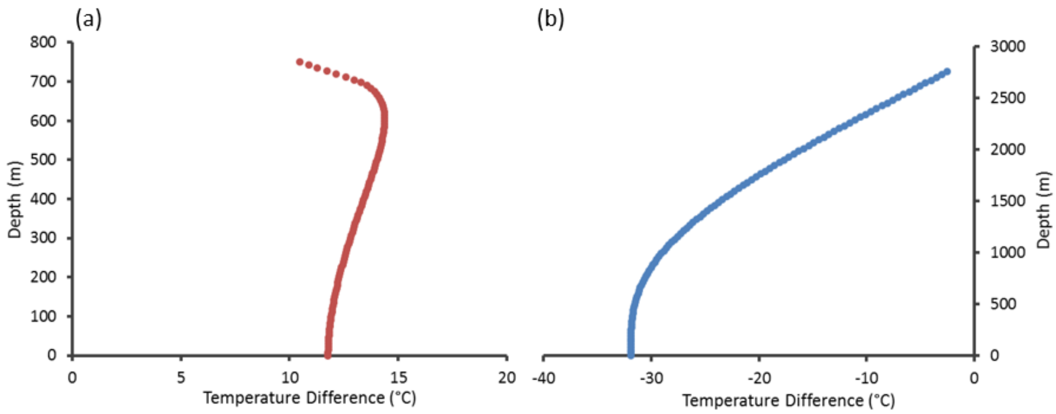

Figure 4.6: Showing the temperature difference of a groundwater recharge scenario (41.3 mm yr^{-1}) versus a non-groundwater recharge (0 mm yr^{-1}) scenario in depth. Graph (a) represents a depth-profile for position x = 0 and (b) for position x = 23490 m.

Further parameters with a crucial meaning for the sensitive analysis of modeled temperature in the subsurface are the porosity, the thermal conductivity of the rock matrix and the bulk thermal conductivity. Previous results were based on a constant porosity value of 10% for the complete model area to keep the model as simple as possible and to focus on groundwater recharge, permeability and heat flow. To estimate the impact of varying porosity values, Figure 4.7 shows scenarios with porosity values of 5% and 25%. This wide range serves to simulate the greatest possible and realistic impact of porosity on modeled temperature. The model results of Figure 4.7 (a) and (b) show higher temperatures for a porosity value of 25%. In contrast to the 5% porosity model scenario the left corner of the

25% porosity model shows a higher temperature gradient. Further, the horizontal colored temperature transition zones are slightly shifted upwards in the 25% model scenario.

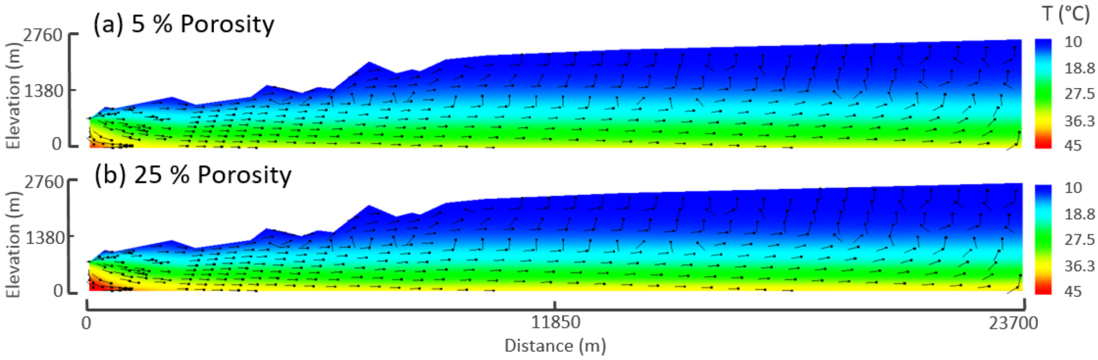

Figure 4.7: Two different rock properties, which are applied in each scenario to every lithological unit. The shown temperature profiles demonstrate the difference between rock properties for the porosity of (a) = 5% and (b) = 25%. Flow vectors demonstrate the groundwater flow directions.

Figure 4.8 (a) and (b) examines the thermal conductivity of the rock matrix. In comparison to snapshot (b) shows snapshot (a) a very pronounced development of temperature in the left corner of the model along with the bottom domain of the model. Furthermore, the snapshot (a) shows a larger cooling-off area which last to a depth of ∼ 1200 m in comparison to snapshot (b). With increasing temperatures starting at 10 °C, we can observe a strongly rising geothermal gradient. In contrast, snapshot (b) increases early, but represents a lower geothermal gradient and only reaches temperature values of approximately 35 °C at the bottom of the model.

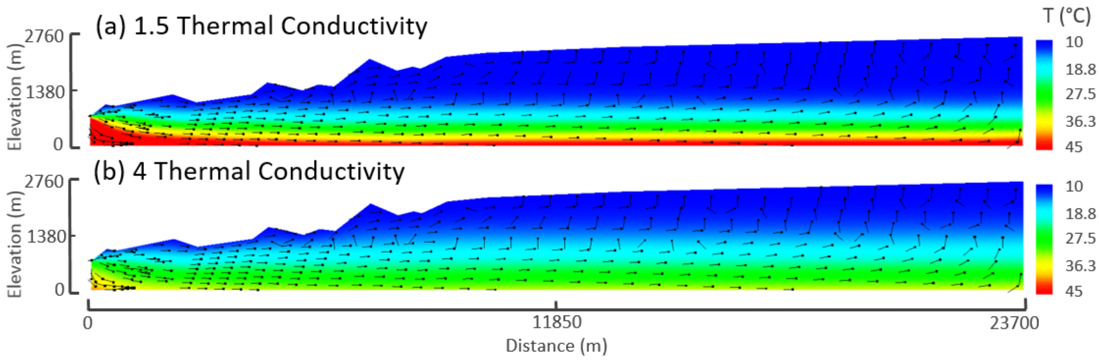

Figure 4.8: Two different rock properties, which are applied in each scenario to every lithological unit. The shown temperature profiles demonstrate the difference between rock properties for the thermal conductivity of the rock matrix (a) = 1.5 and (b) = 4. Flow vectors demonstrate the groundwater flow directions.

Explanations for these temperature variations might be the interaction of the heat flow boundary condition at the bottom domain and the thermal conductivity values. Higher thermal conductivities result in a cooling effect, whereas lower thermal conductivities result in an increase of temperature.

Figure 4.9 demonstrates the relation of hydraulic head versus depth for positions (a) x = 0 m and (b) x = 23490 m. Graph (a) shows a groundwater flow upwards. The groundwater flow for graph (b) indicates a downward trend, which encounters an area of fewer calculation points which is due to the less permeable zone of the Bright Angel Shale. The effect of the low permeability aquiclude (Bright Angel Shale) can be seen in Figure 4.9 (b), as the the hydraulic head is decreasing from the top of the shale to the base of the shale from 3000 m to 1000 m respectively. The velocity vectors in Figure 4.1 clearly show that discharge of fluids is guided by the aquiclude towards the Canyon. Moreover, the aquiclude acts as a low permeability cap prohibiting high fluid flow across the Bright Angel Shale.

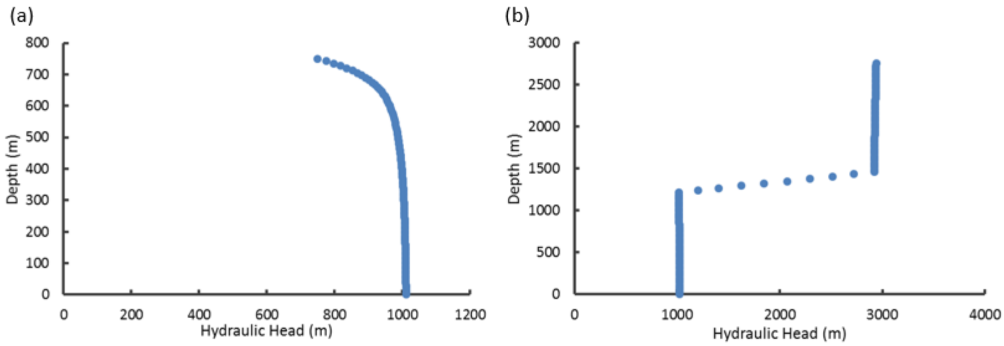

Figure 4.9: Two hydraulic head versus depth plots, showing the potential energy of the water for positions of (a) x = 0 m and (b) x = 23490 m in the model domain.

In Figure 4.10, the Velocity of the groundwater is plotted against the depth at position (a) x = 0 m and (b) x = 23490. Here, positive values correspond to upward groundwater flow and negative values to downward groundwater flow. On the one hand, graph (a) describes increasing velocities towards the upper model domain due to the discharge area. On the other hand, graph (b) slows down from top to bottom on the basis of groundwater recharge at the surface. Smaller fluctuations in the course of the graph (b) can be explained by deviation in permeability of the lithological units. Moreover, the outliners seen in graph (a) and (b) are caused by numerical instability of the model.

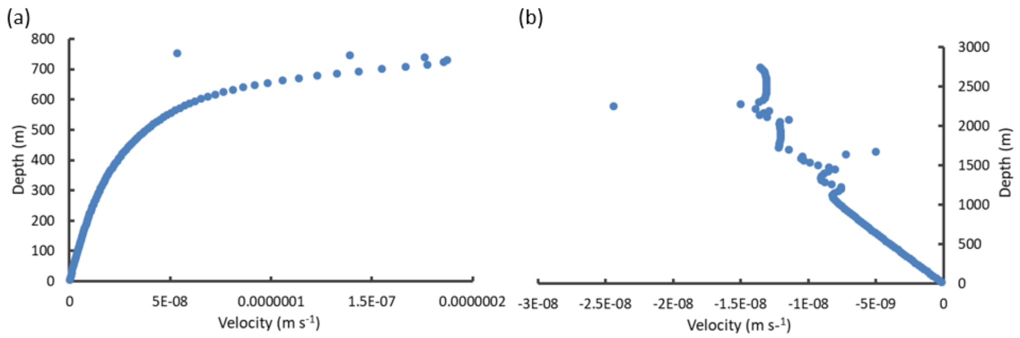

Figure 4.10: Velocity-Depth relationship for position (a) x = 0 m and (b) x = 23490 in the model domain. Graph (a) shows increasing velocities towards the upper model domain, whereas the graph (b) slows down towards the bottom model domain.

4.3 Groundwater flow in the Pleistocene

To quantify the impact on the temperature field, I examined the influence of groundwater recharge, as well as the amount of groundwater recharge which feeds the model. Figure 4.11 and 4.12 represent six model scenarios with groundwater recharges of 20(a), 40(b), 80(c), 120(d), 160(e) and 200(f) mm yr^{-1}.

Comparing these groundwater recharge scenarios, it is noticeable that temperature decreases towards the bottom of the model. This cooling effect increases with groundwater recharge and appears along the entire model length. The discharge area close to the Colorado River is also affected but not to such a great extent. Additionally, this evolution of scenarios reflects a more and more groundwater dominated system. The Scenarios of Figure 4.12 (e) and (f) should be highlighted, since these correspond to late Pleistocene groundwater recharge conditions (*Zhu et al.*, 2003). Moreover, the lower geothermal gradients with values of $\sim$ 23 °C/km and $\sim$ 6 °C/km at locations of x = 0 m and 23490 m locations, in contrast to present-day geothermal gradients with values of $\sim$ 28 °C/km and $\sim$ 10 °C/km confirm previous observed evolutions. It can be noted that the surface boundary condition of groundwater recharge for the plateau area is decisive for the change of temperature from top to bottom of the model.

Figure 4.13 which describes the relation between groundwater recharge and average temperature, confirms that we have a cooling effect of temperature with increasing groundwater recharge into the numerical model. The horizontal lines are representative for the present and past-day groundwater recharge conditions and clarify the difference in cooling between both scenarios.

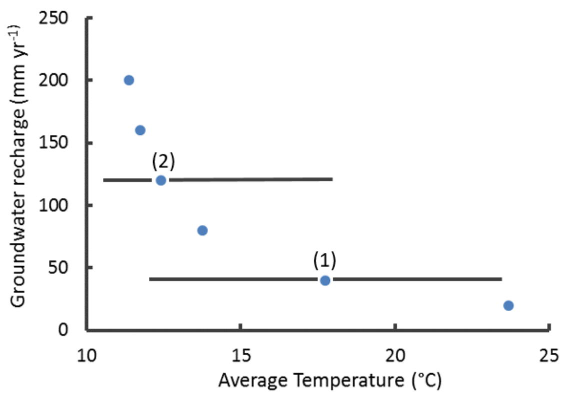

Figure 4.11: Modeled groundwater recharge scenarios versus average temperature using temperature profile at position x = 23490 m. Horizontal lines are showing the estimated values for present-day (1) and Pleistocene (2) groundwater recharge scenarios.

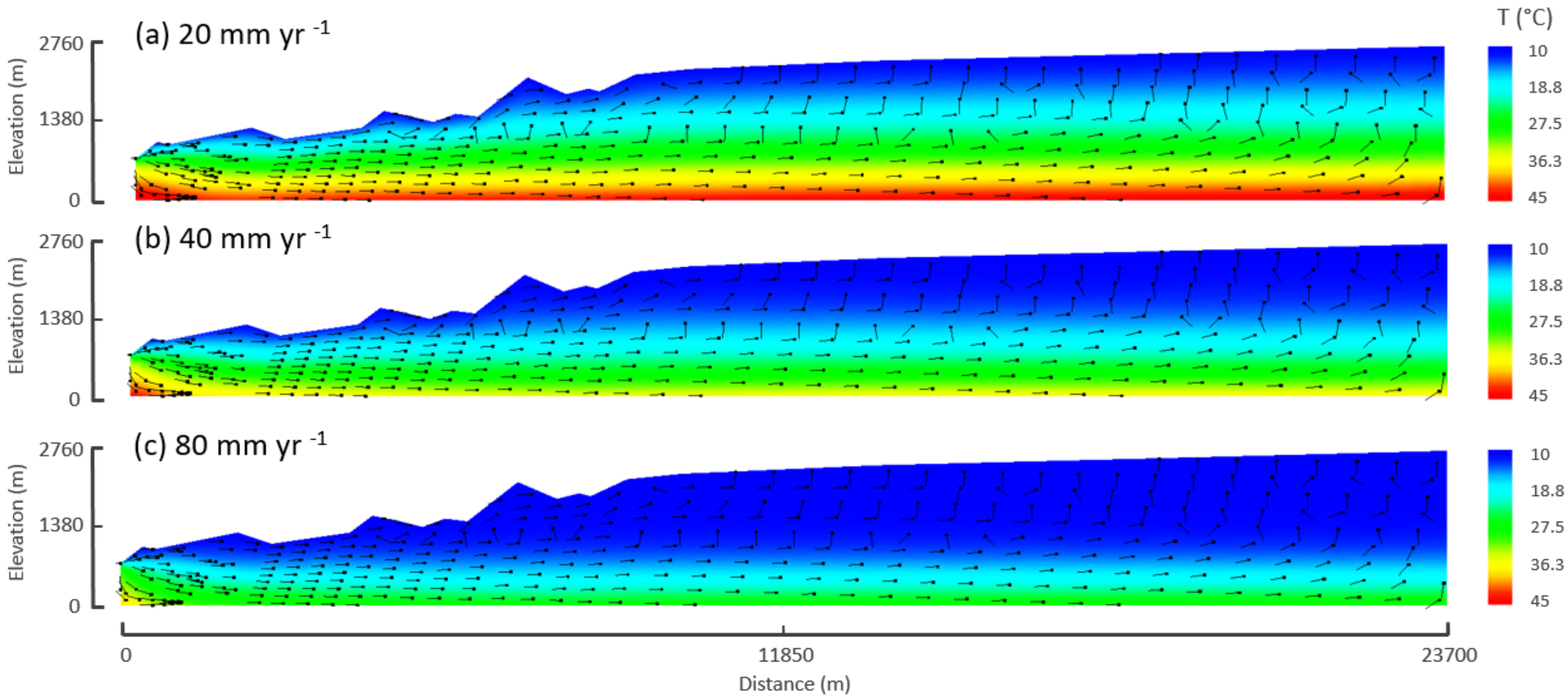

Figure 4.12: Modeled groundwater flow and temperature trends for groundwater recharge scenarios of (a) 20 mm yr^{-1}, (b) 40 mm yr^{-1} and (c) 80 mm yr^{-1}. Flow vectors demonstrate the groundwater flow directions.

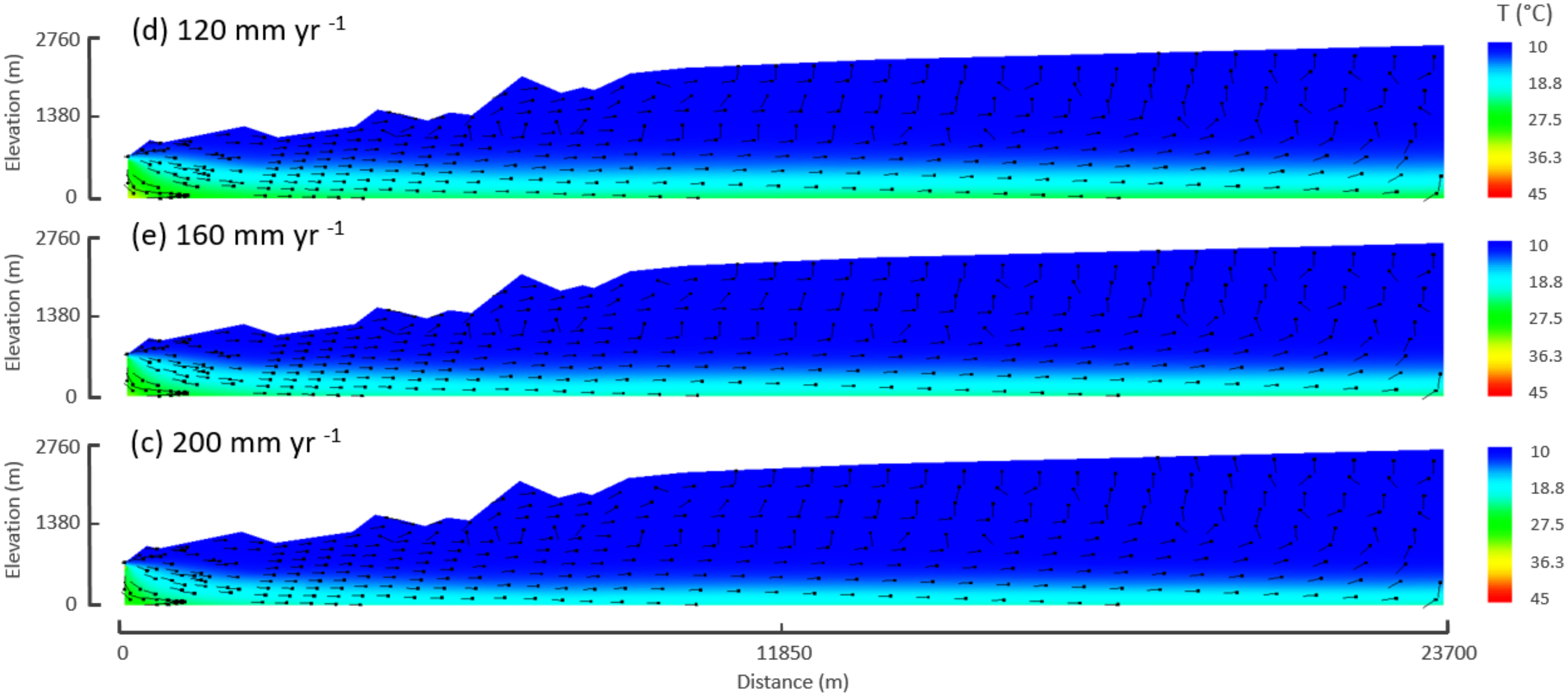

Figure 4.13: Modeled groundwater flow and temperature trends for groundwater recharge scenarios of (d) 120 mm yr^{-1}, (e) 160 mm yr^{-1} and (f) 200 mm yr^{-1}. Scenario (d) and (e) represent the groundwater flow in the Pleistocene (*Zhu et al.*, 2003). Flow vectors demonstrate the groundwater flow directions.

5 Discussion

The model approach (Table 4.2) shows a good fit for the calibration of permeabilities of present-day condition using modeled and measured discharge. Figure 6 indicates the distribution of temperature for the whole model domain as well as the flow direction of the groundwater system is represented by the flow vectors. The conduction of heat is heterogeneous, since the model undergoes advective cooling almost exclusively which is due to the topography-driven groundwater flow spreading consistently into the depth of the model. In contrast, the left margin of the model is heated which is due to the upwards flow caused by discharges into the Colorado River and the Dragon spring (Figure 4.9). Although simulations of Figure 4.4 demonstrate that the permeability near to the discharge sources is highly sensitive leading to different flow paths and other discharge locations.

The comparison of a none and existent groundwater recharge scenario shows that the groundwater recharge significantly changes the temperature field of the model. First, the linear temperature field (Figure 4.5) alters into a heterogeneous temperature field. Second, the best-model fit has an average cooling rate of up to 32 °C at the bottom of the model and the heating in the discharge area suggest temperatures of approximately 14 °C. By simulations of increasing groundwater recharge (Figure 4.12 & 4.13) we ensure past-time groundwater recharge scenarios. Shown results in previous mentioned figures in addition to figure 4.11 indicate a cooling effect that increases with higher groundwater recharge values. This evolution can be also described by decreasing geothermal gradients from $\sim$ 28 °C/km to $\sim$ 23 °C/km and from $\sim$ 10 °C/km to $\sim$ 6 °C/km for locations of x = 0 m and 23490 m. Further changes in temperature and their associated implications can be obtained, if the values of porosity and thermal conductivity are set differently (Figure 4.7 & 4.8). In comparison to porosity value of 5%, a value of 25% result in higher temperature increase in the discharge area. Porosity values of 25% show in the discharge area a higher temperature increase in comparison to porosity value of 5%. The thermal conductivity show with 1.5 higher temperature increases along the model domain, and especially in the discharge area in comparison to the scenario with a thermal conductivity with a value of 4. Simulations for the thermal conductivity of the rock matrix result in higher temperature increases for a value of 1.5 compared to a value of 4. This temperature behaviour is due to the greater interaction between the heat flow boundary condition at the bottom of domain and a lower bulk rock thermal conductivity.

Furthermore, the groundwater recharge values for the best model fit vary a lot (see section 4.1). The range between the measured (*ADWR*, 2009) 41.3 mm yr^{-1} and the calculated global scale models with 5 and 14.3 mm yr^{-1} from *De Graaf et al.* (2015) and *Wolock* (2003) differ a lot in this model which can be due to implications of arid climate conditions. Above all, the parameter of groundwater recharge implies a significant role in space and time. The thermal system without groundwater mainly consist of an original presumed basal heat flow as sole heat conductor that shifts towards a system that adds a groundwater dominated cooling component by topography-driven groundwater flow. Nevertheless, we experience heating due to upwards flow of groundwater in the discharge area. The impact of the strongly related groundwater recharge is higher for past – times (Pleistocene) in comparison to present-day, which should be considered for assumptions of exhumations rates at the time of formation.

6 Conclusion

In this study a 2-D numerical model of groundwater and heat flow for a specific cross-section of the Grand Canyon is presented. To reproduce lithological characteristics for present-day conditions a relatively simple method is successfully used; available spring discharge data of the study area is adjusted to modeled spring discharge data by calibrating permeability values for each geologic unit. The best-model fit shows a topography-driven groundwater flow system that strongly affects the temperature field of the subsurface. The modeled temperature field shows a cooling effect up to 32 °C at the bottom of the model which occurs for almost the entire model lenght with exception of the discharge area close to the Colorado River. Besides this, the groundwater experiences a heating of $\sim$ 14 °C at the left margin due to the upwards flow towards discharge sources. Here, the geothermal gradient can also vary, if the highly sensitive permeability is slightly changed and the groundwater system discharges more through the Colorado River than through the spring.
By choosing fixed values of 10% and 3.5 for parameters of the porosity and thermal conductivity, the model setup ensures a simplified calibration only by means of permeability which nonetheless remains realistic. The thermal effect of previously mentioned parameters are also simulated and should not be neglected but are not heterogeneously implemented into the calibrated model. Furthermore, the comparison of a none and existent groundwater recharge scenario highlights the thermal effects. A system without groundwater recharge consists of a linear heat conductivity caused by a basal heat flow, whereas present groundwater recharge leads to advective cooling by topography-driven groundwater flow and heating by upwards groundwater flow. The simulation results with higher groundwater recharge scenarios demonstrate increasing topography-driven groundwater flow that leads to a greater cooling effect and therefore to a greater thermal effect in times of the Pleistocene. Geothermal gradients in space and time confirm the observed temperature evolutions. The geothermal gradient of the discharge area close to the Colorado River decreases from $\sim$ 28 °C/km to $\sim$ 23 °C/km and the geothermal gradient for the plaetau area decreases from $\sim$ 10 °C/km to $\sim$ 6 °C/km for the present to past-day groundwater recharge conditions.
In conclusion, the results points strong thermal effects that are related to topography-driven groundwater flow. Special attention should be given to the heterogonous temperature field which implies a cooling for almost the entire model with exception for the discharge area around the Colorado River which undergoes heating. Additionally, greater groundwater recharge scenarios suggest that the thermal effects were even more signifi-

cant in the past. Thus, the results show that groundwater and heat flow with altering temperatures in time and space plays an important role in the thermal history and should be included in studies regarding the time of formation for the Grand Canyon that rely almost exclusively on low-temperature thermochronology.

The model simulations can be seen as a first-order attempt towards groundwater and heat flow modeling with regards to the influence of thermal effects. However, they have their limitations that hamper a completely trustworthy simulation. Further investigations should aim to improve the parametrizations of the model to capture the full structural complexity. Terms which should be considered are: heterogeneities of layers, faults and their location, spreading of sinkholes and joints, specified porosities for each layer instead of a simplified model-wide value as well as the chemical composition of aqueous fluids.

Bibliography

ADWR, A. D. o. W. R. (2009), *Arizona Water Atlas Volume 6 Western Plateau Planning Area*, 297 pp., available at `http://www.azwater.gov/AzDWR/StatewidePlanning/WaterAtlas/WesternPlateau/default.htm`, last accessed on 08.09.2017.

Anderson, M. P. (2005), Heat as a Ground Water Tracer, *Ground Water*, *43*(6), 951–968, doi:10.1111/j.1745-6584.2005.00052.x.

Bense, V. F., T. Gleeson, S. E. Loveless, O. Bour, and J. Scibek (2013), Fault zone hydrogeology, doi:10.1016/j.earscirev.2013.09.008.

Beus, S. S., and M. Morales (2003), *Grand Canyon Geology*, 432 pp., Oxford University Press.

Carman, P. C. (1937), Fluid flow through granular beds, *Institution of Chemical Engineeres*.

De Graaf, I. E. M., E. H. Sutanudjaja, L. P. H. Van Beek, and M. F. P. Bierkens (2015), A high-resolution global-scale groundwater model, *Hydrology and Earth System Sciences*, *19*(2), 823–837, doi:10.5194/hess-19-823-2015.

Durner, W. (1994), Hydraulic conductivity estimation for soils with heterogeneous pore structure, *Water Resources Research*, *30*(2), 211–223, doi:10.1029/93WR02676.

Farley, K. A. (2000), Helium diffusion from apatite: General behavior as illustrated by Durango fluorapatite, *Journal of Geophysical Research: Solid Earth*, *105*(B2), 2903–2914, doi:10.1029/1999JB900348.

Foos, A. (1999), Geology of Grand Canyon National Park , North Rim.

Freeze, R. A., and J. A. Cherry (1979), *Groundwater*, 1–624 pp.

Gleeson, T., L. Smith, N. Moosdorf, J. Hartmann, H. H. Dürr, A. H. Manning, L. P. H. Van Beek, and A. M. Jellinek (2011), Mapping permeability over the surface of the Earth, *Geophysical Research Letters*, *38*(2), 1–6, doi:10.1029/2010GL045565.

Hill, C. A., and V. J. Polyak (2010), Karst hydrology of Grand Canyon, Arizona, USA, *Journal of Hydrology*, doi:10.1016/j.jhydrol.2010.06.040.

Hill, C. A., et al. (2016), *The Grand Canyon : monument to an ancient Earth : can Noah's flood explain the Grand Canyon?*

Huntoon, P. W. (1974), The karstic groundwater basins of the Kaibab Plateau, Arizona, *Water Resources Research*, *10*(3), 579–590, doi:10.1029/WR010i003p00579.

Huntoon, P. W. (2000a), Karstification associated with groundwater circulation through the Redwall Artesian Aquifer, Grand Canyon, Arizona.

Huntoon, P. W. (2000b), Variability of karstic permeability between unconfined and confined aquifers, Grand Canyon region, Arizona, *Environmental & Engineering Geoscience*, *6*(2), 155–170, doi:10.2113/gseegeosci.6.2.155.

Ingraham, N. L., K. Zukosky, and D. K. Kreamer (2001), Application of Stable Isotopes To Identify Problems in Large-Scale Water Transfer in Grand Canyon National Park, doi:10.1021/ES0015186.

Irvine, D. J., R. H. Cranswick, C. T. Simmons, M. A. Shanafield, and L. K. Lautz (2015), The effect of streambed heterogeneity on groundwater-surface water exchange fluxes inferred from temperature time series, *Water Resources Research*, *51*(1), 198–212, doi:10.1002/2014WR015769.

Karlstrom, K. E., R. Crow, L. J. Crossey, D. Coblentz, and J. W. Van Wijk (2008), Model for tectonically driven incision of the younger than 6 Ma Grand Canyon, *Geology*, *36*(11), 835, doi:10.1130/G25032A.1.

Karlstrom, K. E., et al. (2014), Formation of the Grand Canyon 5 to 6 million years ago through integration of older palaeocanyons, doi:10.1038/NGEO2065.

Keshari, A. K., and M. Koo (2007), A numerical model for estimating groundwater flux from subsurface temperature profiles, *Hydrological Processes*, *21*(25), 3440–3448, doi:10.1002/hyp.6577.

Ketcham, R. A., A. Carter, R. A. Donelick, J. Barbarand, and A. J. Hurford (2007), Improved modeling of fission-track annealing in apatite, *American Mineralogist*, *92*(5-6), 799–810, doi:10.2138/am.2007.2281.

Kozeny, J. (1927), Uber Kapillare Leitung der Wasser in Boden, *Royal Academy of Science, Vienna, Proc. Class I*, *136*, 271–306.

Kumar, C. P. (2012), Climate Change and Its Impact on Groundwater Resources, *1*(5), 43–60.

Metzger, D. G. (1961), Geology in Relation to Availability of Water Along the South Rim Grand Canyon National Park Arizona, *US Government Printing Office*.

Neuzil, C. E. (1994), by Bethke permeability , measurements in Figure, *Water Resources*, *30*(2), 145–150.

Pollack, H. N., S. J. Hurter, and J. R. Johnson (1993), Heat flow from the Earth's interior: Analysis of the global data set, *Reviews of Geophysics*, *31*(3), 267, doi: 10.1029/93RG01249.

Price, L. G. (1999), *An introduction to Grand Canyon geology*, 63 pp., Grand Canyon Association.

Shuster, D. L., and K. A. Farley (2004), 4He/3He thermochronometry, *Earth and Planetary Science Letters*, *217*(1-2), 1–17, doi:10.1016/S0012-821X(03)00595-8.

USGS, U. S. G. S. (2013), National Elevation Dataset, available at `https://lta.cr.usgs.gov/NED`, last accessed on 07.07.2017.

Voss, . I., and A. M. Provost (2010), SUTRA: a model for saturated-unsaturated, variable-density ground-water flow with solute or energy transport, *Water-Resources Investigations Report 02-4231*, *2010*, 300 p.

Wernicke, B. (2011), The California River and its role in carving Grand Canyon, *Geological Society of America Bulletin*, *123*(7-8), 1288–1316, doi:10.1130/B30274.1.

Wolock, D. M. (2003), Estimated mean annual natural ground-water recharge in the conterminous United States, *U.S. Geological Survey*, (Open-File Rep 03–311, digital dataset), available at `https://pubs.er.usgs.gov/publication/ofr03311`, last accessed on 07.07.2017.

Zhu, C., R. K. Waddell, I. Star, and M. Ostrander (1998), Responses of ground water in the Black Mesa basin, northeastern Arizona, to paleoclimatic changes during the late Pleistocene and Holocene, *Geology*, *26*(2), 127, doi:10.1130/0091-7613(1998)026⟨0127:ROGWIT⟩2.3.CO;2.

Zhu, C., J. R. Winterle, and E. I. Love (2003), Late Pleistocene and Holocene groundwater recharge from the chloride mass balance method and chlorine-36 data, *Water Resources Research*, *39*(7), doi:10.1029/2003WR001987.

7 Appendix

Appendix Table .1: Modeled discharge values of the Colorado River and the Dragon spring for the Redwall-Muav-Aquifer at specific logk values.

Redwall-Muav-Aquifer

Dragon Spring	Colorado River	logk (m^2)
-3.956E-02	-4.173E-01	-10.3
-3.956E-02	-4.173E-01	-10.6
-3.957E-02	-4.173E-01	-10.9
-3.957E-02	-4.173E-01	-11.2
-3.957E-02	-4.174E-01	-11.5
-3.957E-02	-4.174E-01	-11.8
-3.957E-02	-4.174E-01	-12.1
-3.957E-02	-4.174E-01	-12.4
-3.957E-02	-4.174E-01	-12.7
-3.957E-02	-4.174E-01	-13
-3.957E-02	-4.174E-01	-13.3

Appendix Table .2: Modeled discharge values of the Colorado River and the Dragon spring for the Bright Angel Shale at specific logk values.

Bright Angel Shale

Dragon Spring	Colorado River	logk (m^2)
-3.958E-02	-4.173E-01	-17.9
-3.958E-02	-4.174E-01	-18.1
-3.957E-02	-4.174E-01	-18.3
-3.957E-02	-4.174E-01	-18.5
-3.957E-02	-4.174E-01	-18.7
-3.957E-02	-4.174E-01	-18.9
-3.957E-02	-4.174E-01	-19.1
-3.957E-02	-4.174E-01	-19.3
-3.957E-02	-4.174E-01	-19.5
-3.957E-02	-4.174E-01	-19.7
-3.957E-02	-4.174E-01	-19.9
-3.957E-02	-4.174E-01	-20.1

Appendix Table .3: Modeled discharge values of the Colorado River and the Dragon spring for the Middle Proterozoic Sedimentary Rocks at specific logk values.

Middle Proterozoic Sedimentary Rocks

Dragon Spring	Colorado River	logk (m^2)
-4.130E-01	-4.389E-02	-12.7
-4.028E-01	-5.417E-02	-12.9
-3.879E-01	-6.905E-02	-13.1
-3.671E-01	-8.979E-02	-13.3
-3.396E-01	-1.173E-01	-13.5
-3.052E-01	-1.517E-01	-13.7
-2.653E-01	-1.916E-01	-13.9
-2.224E-01	-2.345E-01	-14.1
-1.800E-01	-2.770E-01	-14.3
-1.411E-01	-3.159E-01	-14.5
-1.077E-01	-3.493E-01	-14.7
-8.041E-02	-3.765E-01	-14.9
-5.891E-02	-3.980E-01	-15.1
-4.236E-02	-4.146E-01	-15.3
-2.986E-02	-4.271E-01	-15.5
-2.060E-02	-4.363E-01	-15.7
-1.392E-02	-4.430E-01	-15.9
-9.235E-03	-4.477E-01	-16.1
-6.034E-03	-4.509E-01	-16.3
-3.897E-03	-4.530E-01	-16.5
-2.497E-03	-4.544E-01	-16.7
-1.591E-03	-4.553E-01	-16.9
-1.010E-03	-4.559E-01	-17.1
-6.394E-04	-4.563E-01	-17.3
-4.041E-04	-4.565E-01	-17.5
-2.551E-04	-4.567E-01	-17.7

Appendix Table .4: Modeled discharge values of the Colorado River and the Dragon spring for the Early Proterozoic Crystalline Rocks at specific logk values.

Early Proterozoic Crystalline Rocks		
Dragon Spring	Colorado River	logk (m^2)
6.227E-07	-4.569E-01	-12.6
-2.562E-06	-4.569E-01	-12.8
-7.588E-06	-4.569E-01	-13
-1.551E-05	-4.569E-01	-13.2
-2.798E-05	-4.569E-01	-13.4
-4.756E-05	-4.569E-01	-13.6
-7.829E-05	-4.568E-01	-13.8
-1.265E-04	-4.568E-01	-14
-2.022E-04	-4.567E-01	-14.2
-3.214E-04	-4.566E-01	-14.4
-5.089E-04	-4.564E-01	-14.6
-8.041E-04	-4.561E-01	-14.8
-1.268E-03	-4.557E-01	-15
-1.993E-03	-4.549E-01	-15.2
-3.121E-03	-4.538E-01	-15.4
-4.858E-03	-4.521E-01	-15.6

Appendix Table .5: Calculation of each heat flow rectangle for the bottom model boundary condition.

Segment length	Quantity	Length (m)	Cell length (m)	Heat flow per rectangle
400	20	400	20	1.3
600	8	200	25	1.625
2100	60	1500	25	1.625
2700	24	600	25	1.625
4100	54	1400	25.92592593	1.685185185
4500	16	400	25	1.625
5000	18	500	27.77777778	1.805555556
5400	14	400	28.57142857	1.857142857
5800	14	400	28.57142857	1.857142857
6200	12	400	33.33333333	2.166666667
7100	26	900	34.61538462	2.25
7800	24	700	29.16666667	1.895833333
8200	13	400	30.76923077	2
8400	7	200	28.57142857	1.857142857
9050	20	650	32.5	2.1125
10050	25	1000	40	2.6
13500	86	3450	40.11627907	2.60755814
15500	50	2000	40	2.6
19500	100	4000	40	2.6
23700	100	4200	42	2.73

Appendix Table .6: Calculation of the 5 groundwater recharge rectangles for the top model boundary condition.

Rectangle	Quantity	Segment length	Cell length
1	25	1000	40
2	86	3450	40.11627907
3	50	2000	40
4	100	4000	40
5	100	4200	42

Appendix Table .7: Groundwater recharge scenarios with their mm yr^{-1} values, the conversion of these and calculated values of each groundwater recharge rectangle at the top model boundary for simulations in Sutra.

	Groundwater recharge							
References	De Graaf et al. 2015	Wolock 2003	ADWR 2009			Zhu et al. 2003		
mm yr^{-1}	5	14.3	41.3	20	80	123.9	160	200
m s^{-1}	1.59E-10	4.53E-10	1.31E-09	6.34E-10	2.54E-09	3.93E-09	5.07E-09	6.34E-09
Rectangle								
1	6.34E-06	1.81E-05	5.23E-05	2.54E-05	1.01E-04	1.57E-04	2.03E-04	2.54E-04
2	6.36E-06	1.82E-05	5.25E-05	2.54E-05	1.02E-04	1.57E-04	2.04E-04	2.54E-04
3	6.34E-06	1.81E-05	5.23E-05	2.54E-05	1.01E-04	1.57E-04	2.03E-04	2.54E-04
4	6.34E-06	1.81E-05	5.23E-05	2.54E-05	1.01E-04	1.57E-04	2.03E-04	2.54E-04
5	6.66E-06	1.90E-05	5.49E-05	2.66E-05	1.07E-04	1.65E-04	2.13E-04	2.66E-04